

Photoelectrochemical Behavior of Nanostructured TiO₂ Thin-Film Electrodes in Contact with Aqueous Electrolytes Containing Dissolved Pollutants: A Model for Distinguishing between Direct and Indirect Interfacial Hole Transfer from Photocurrent Measurements

Iván Mora-Seró,[†] Teresa Lana Villarreal,^{‡,§} Juan Bisquert,[†] Ángeles Pitarch,[†] Roberto Gómez,[§] and Pedro Salvador^{*,‡,||}

Departament de Ciències Experimentals, Universitat Jaume I, 12080 Castelló, Spain, Instituto de Catálisis y Petroleoquímica, CSIC, Madrid, Spain, Departament de Química Física i Institut Universitari d'Electroquímica, Universitat d'Alacant, Ap. 99, E-03080 Alacant, Spain, and Departament de Matemàtiques i Informàtica, Universitat de les Illes Balears, E-07122, Spain

Received: September 29, 2004; In Final Form: November 24, 2004

A model for describing the photoelectrochemical behavior of nanostructured TiO₂ thin-film electrodes in contact with aqueous electrolytes containing dissolved pollutant species is presented. The model correlates the steady-state photocurrent, the illumination intensity, and the specific photooxidation mechanism for dissolved pollutant species in competition with water molecules. For physical events, the model considers the existence of hole trapping at surface states and the specific hole-transfer mechanisms taking place at the semiconductor–electrolyte interface (direct, via photogenerated valence-band free holes or indirect, via photogenerated surface-bound OH radicals or both). The model has been applied to the study of the photooxidation of aqueous solutions of formic acid and methanol. In agreement with previous results concerning massive polycrystalline electrodes, methanol is found to be photooxidized via indirect hole transfer, whereas formic acid is photooxidized mainly with the participation of valence-band free holes.

1. Introduction

Semiconductor photocatalysts have been investigated intensively because of their applicability in the treatment of wastes and pollutants in air and water.^{1–5} The initial photooxidation processes occurring immediately after illumination are, however, not clearly understood. Because the photocatalytic reactions proceed in an aqueous environment, surface-bound OH_s[•] radicals are initially photogenerated via direct reaction of valence-band free holes with chemisorbed water molecules.⁵ These hydroxyl radicals are able to oxidize dissolved pollutant species (indirect photooxidation mechanism). Alternatively, pollutant species can be oxidized directly by reaction with photogenerated valence-band free holes (direct photooxidation mechanism).⁶ Recently Villarreal et al. have developed a kinetic model that is able to discriminate between both mechanisms by photoelectrochemical measurements involving dense, polycrystalline, or single-crystal electrodes.⁷ This model considers both the “current multiplication” and negligible recombination of photogenerated electron-hole pairs, the latter being consistent with the existence of an electric field (band bending) at the semiconductor–electrolyte interface, which can be neutralized under external polarization of the photoelectrode.

The interest in using nanostructured electrodes in photocatalytic water-decontamination applications has increased lately. On one hand, the use of supported semiconductor nanoparticles provides thin-film photoelectrodes with a specific surface area

that is several orders of magnitude higher than that of polycrystalline or single-crystal electrodes,^{8,9,12,13} which facilitates interfacial charge-transfer reactions considerably. On the other hand, the awkward separation processes that are required when using suspensions of nanoparticles are avoided.¹⁰ Moreover, the efficiency of the decontamination process can be improved by applying a bias.¹¹ TiO₂ nanoparticles that are immobilized on a transparent, conducting substrate may enjoy these advantages.

2. Model

A complete analysis of the photoelectrochemical behavior of nanostructured electrodes involves the knowledge of both electron transport and interfacial charge-transfer processes. Because diffusion is the main transport mechanism for photogenerated electrons through the nanostructured network, the diffusion equation should be solved to calculate the photocurrent intensity that is flowing through the external circuit. On the basis of these premises, a kinetic model has been developed to describe the photoelectrochemical behavior of nanostructured thin-film electrodes in contact with aqueous electrolytes containing dissolved pollutants. This model not only establishes relationships between the steady-state photocurrent intensity, the illumination intensity, and the concentration of dissolved pollutant species but also is able to determine whether direct or indirect interfacial hole transfer to the solute predominates.

Before describing our model, let us outline the pioneer approach by de Jongh and Vanmaekelbergh (dJV),^{14,15} which provides an approximate solution under certain limiting conditions. dJV discussed the electronic processes that determine the photoelectrochemical behavior of nanostructured semiconductor electrodes in contact with indifferent aqueous electrolytes. These authors considered the existence of both internal traps, which are able to influence electron transport by trapping and thermal

* Corresponding author. Address: Departament de Ciències Matemàtiques i Informàtica, Universitat de les Illes Balears, Ctra. de Valldemossa Km. 7.5, E-07122 Palma de Mallorca, Spain. Tel: +34 971 172962. Fax: +34 971 173003. E-mail: dmipss9@uib.es.

[†] Universitat Jaume I.

[‡] CSIC.

[§] Universitat d'Alacant.

^{||} Universitat de les Illes Balears.

release, and surface states mediating interfacial electron transfer. Because we are interested in the steady-state behavior of the photocurrent, which is related to the opto-electrical transfer function in the zero-frequency limit, the effect of internal traps can be considered to be irrelevant,^{16,17} and the diffusion coefficient, D , corresponding to the transport of conduction-band electrons can be considered to be constant.^{16,17}

Let us outline the implications of the dJV model with respect to the light-intensity dependence of the steady-state photocurrent. The model can be formulated in terms of three equations:¹⁵

(1) The continuity equation for free electrons photogenerated at a rate $\alpha\Phi(x)$

$$\frac{\partial n}{\partial t} = \alpha\Phi - \frac{\partial J}{\partial x} - \beta_R n(1 - f_R) \quad (1)$$

where α is the absorption coefficient, $\Phi(x) = \Phi_0 e^{-\alpha x}$, with Φ_0 as the incident photon flux, $n(x, t)$ is the conduction-band free-electron density within the film at a distance x from the illuminated film face at any time t , $J(x, t)$ is the electron flux, f_R is the electron occupancy factor of the trap level denoted by R and β_R is the probability for electron trapping.

(2) The equation of conservation of valence-band free holes

$$\frac{\partial p}{\partial t} = \alpha\Phi - \beta_p f_R p \quad (2)$$

where p is the hole concentration and β_p is the hole-trapping probability.

(3) The equation of conservation of the conduction-band electrons trapped at the surface states

$$\frac{\partial f_R}{\partial t} = [\beta_R n + k'_{\text{red}}][1 - f_R] - \beta_p f_R p \quad (3)$$

where k'_{red} is the interfacial electron-transfer rate.

For clarity, we will express eqs 1–3 in terms of f_h , the occupancy of the holes at trap level R , so that

$$\frac{\partial n}{\partial t} = \alpha\Phi - \frac{\partial J}{\partial x} - \beta_R n f_h \quad (4)$$

$$\frac{\partial p}{\partial t} = \alpha\Phi - \beta_p p(1 - f_h) \quad (5)$$

$$\frac{\partial f_h}{\partial t} = -[\beta_R n + k'_{\text{red}}]f_h + \beta_p p(1 - f_h) \quad (6)$$

At the steady state ($\partial X/\partial t = 0$, for any variable X), we obtain from eqs 5 and 6

$$f_h = \frac{\alpha\Phi}{\beta_R n + k'_{\text{red}}} \quad (7)$$

so that the recombination rate (removal of electrons from the conduction band), which is given by the third term of eq 4, can be expressed as

$$U(n) = \frac{\beta_R n}{\beta_R n + k'_{\text{red}}} \alpha\Phi \quad (8)$$

Moreover, from eqs 4 and 7, the following relationship between the local flux, the free-electron concentration, and the illumination intensity is obtained

$$\frac{\partial J}{\partial x} = \frac{k'_{\text{red}}}{\beta_R n + k'_{\text{red}}} \alpha\Phi \quad (9)$$

Two limiting cases can be considered in eq 9: (a) negligible recombination ($\beta_R n \ll k'_{\text{red}}$), so that

$$\frac{\partial J}{\partial x} = \alpha\Phi \quad (10)$$

and (b) predominant recombination ($\beta_R n \gg k'_{\text{red}}$), so that

$$\frac{\partial J}{\partial x} = \frac{k'_{\text{red}}}{\beta_R n} \alpha\Phi \quad (11)$$

To derive the steady-state electron flux collected at the back contact (i.e., the photocurrent density), we should solve the transport equations under appropriate boundary conditions. However, on the basis of a linear dependence of J on n , a simple qualitative analysis shows the main features of the photocurrent with respect to the illumination intensity. In fact, from eq 10, it follows that

$$J(x) \propto n(x) \propto \alpha\Phi(x) \quad (12)$$

Because eq 12 is also valid at the back contact ($x = 0$ under back contact illumination), the electron flux at the back contact (photocurrent intensity) will be $J(0) \propto \Phi_0$, which means that every photogenerated electron is extracted at the back contact, whereas every hole is injected into the solution, as it should be in the absence of recombination. By contrast, when recombination is predominant, eq 11 implies that

$$J(x) \propto n(x) \propto (\alpha\Phi(x))^{1/2} \quad (13)$$

and for $x = 0$, $J(0) \propto (\alpha\Phi_0)^{1/2}$, so a linear plot of $\log(J(0))$ versus $\log(\Phi_0)$ with a slope of 0.5 is obtained. It should be noted that the square-root photocurrent intensity dependence on Φ of eq 13 has been obtained in the framework of a first-order recombination reaction, which is implicit in the third term of eq 4. A similar dependence is obtained if we consider a second-order recombination reaction, as suggested for the case of dye-sensitized solar cells.¹⁸

Let us now analyze the differences between our approach and the dJV approach. These authors use the following expression for the electron flux

$$J = \mu_n \epsilon_F n \quad (14)$$

where the driving force ϵ_F for the drift of photogenerated electrons through the network is the gradient of Fermi level and μ_n is the electron mobility. Because ϵ_F is considered to be independent of x , we have that

$$\frac{\partial J}{\partial x} = \mu_n \epsilon_F \frac{\partial n}{\partial x} \quad (15)$$

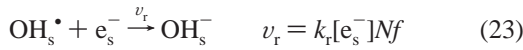
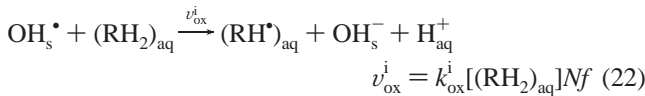
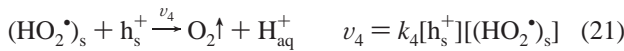
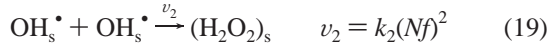
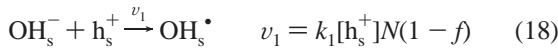
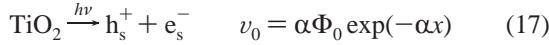
With the help of eq 15, eqs 10 and 11 can be integrated, and eqs 12 and 13 can be confirmed. However, we prefer to adopt the expression for the diffusion flux given by Fick's first law

$$J(x) = -D \frac{\partial n}{\partial x} \quad (16)$$

where D is the diffusion coefficient for electrons. Equation 16 determines the electron flux at the back contact (i.e., the photocurrent intensity). To solve eq 16, we need to know $n(x)$, which is obtained by solving the diffusion equation. But this

implies a precise knowledge of the mechanisms of surface recombination and interfacial transfer of charge. In addition, while the dJV model considers a single mechanism of interfacial hole transfer to unspecified species in solution, we distinguish between indirect and direct interfacial hole transfer to water-dissolved species.⁷

2.1. Indirect Interfacial Hole Transfer. The indirect hole-transfer model takes into account the following sequence of reactions:⁷



where $N = [\text{OH}_s^-]_{\text{in}}$, $Nf = [\text{OH}_s^\bullet]$, and $N(1-f) = [\text{OH}_s^-]$.

Equation 17 represents the photogeneration of electron–hole pairs with photons of energy equal to or greater than the band-gap energy (x represents the distance to the illuminated face) at a rate ν_0 . Equation 18 represents the trapping of photogenerated valence-band free holes at surface-bound hydroxide ions (or alternatively water molecules) with their surface concentration under equilibrium conditions in the dark being $[\text{OH}_s^-]_{\text{in}} = N$. The concentration of surface-bound OH_s^\bullet radicals ($[\text{OH}_s^\bullet]$) is represented by Nf with f being the surface coverage so that $[\text{OH}_s^-] = N(1-f)$, as far as $[\text{OH}_s^-] + [\text{OH}_s^\bullet] \approx [\text{OH}_s^-]_{\text{in}}$.⁷ Equation 19 indicates the surface generation of hydrogen peroxide $(\text{H}_2\text{O}_2)_s$ through the combination of two neighboring surface-bound photogenerated OH_s^\bullet radicals. This reaction is the limiting step of water photooxidation (O_2 evolution).²⁴ Further photooxidation of the $(\text{H}_2\text{O}_2)_s$ species gives rise to $(\text{HO}_2^\bullet)_s$ radicals (eq 20), which are further oxidized to O_2 (eq 21). Photogenerated OH_s^\bullet radicals can also react with $(\text{RH}_2)_{\text{aq}}$ dissolved pollutant species (eq 22), giving rise to RH^\bullet oxidized species. OH_s^\bullet radicals (surface-trapped holes) can also recombine with photogenerated conduction-band free electrons, as assumed by eq 23. Finally, eq 24 represents the current-doubling phenomenon associated with the direct injection of electrons from the RH^\bullet radical species photogenerated in step 22 into the conduction band. Because the desorption of hydroxyl radicals into the solution is unlikely,²⁵ reactions involving free OH are not considered.⁷

All of the rates in eqs 18–24 are expressed in $\text{cm}^{-2} \text{s}^{-1}$ (or alternatively in $\text{mol} \cdot \text{cm}^{-2} \text{s}^{-1}$) and therefore are measured per unit of real (inner) surface area of the porous film. However, the carrier generation rate, ν_0 , in eq 17 is measured in $\text{cm}^{-3} \text{s}^{-1}$ (or $\text{mol} \cdot \text{cm}^{-3} \text{s}^{-1}$). That is, it is measured per unit of nanoporous film volume (including both pores and particles). Therefore, a

conversion factor, B (cm), needs to be introduced into eqs 18–24 in order to homogenize the reaction rates.²⁶ B can be approximated by the ratio V/S , where V refers to the total volume of the thin film and S refers to its inner surface area (B is on the order of the particle size).

Under steady-state conditions, we have that

$$\nu_0 = \frac{1}{B}(\nu_1 + \nu_3 + \nu_4) \quad (25)$$

$$\nu_2 = \nu_3 = \nu_4 \quad (26)$$

$$\nu_{\text{red}}' = \nu_{\text{ox}}^i \quad (27)$$

$$\nu_1 = 2\nu_2 + \nu_{\text{ox}}^i + \nu_r \quad (28)$$

From eqs 17–28, Nf can be obtained as

$$Nf = \frac{-(e_{\text{ox}}^i + k_r n) + \sqrt{(e_{\text{ox}}^i + k_r n)^2 + 16k_2 B \alpha \Phi_0 \exp(-\alpha x)}}{8k_2} \quad (29)$$

where $n \equiv [\text{e}_s^-]$ is the concentration of conduction-band free electrons and $e_{\text{ox}}^i = k_{\text{ox}}^i[(\text{RH}_2)_{\text{aq}}]$. Assuming that diffusion is the main electron-transport mechanism, the continuity equation can be written as

$$\frac{\partial n(x, t)}{\partial t} = -\frac{\partial J(x, t)}{\partial x} + G(x, t) - R(x, t) \quad (30)$$

where G and R are the carrier generation rate and surface recombination rate, respectively. Let n_0 be the conduction-band electron concentration under equilibrium conditions in the dark. Note that even for low illumination intensities $n - n_0 \approx n$, so for practical purposes, n_0 can be suppressed. By solving eq 30, we will obtain $n(x)$. Under current multiplication (doubling), the generation rate can be written as $G = \alpha\Phi_0 \exp(-\alpha x) + (e_{\text{ox}}^i Nf)/B$. Moreover, if eq 23 is considered to be the only recombination pathway, it must be that $R = (k_r Nf)/B$, so the time-dependent transport equation for electrons becomes

$$-\frac{\partial J(x, t)}{\partial x} - \frac{\partial n(x, t)}{\partial t} + \alpha\Phi_0 \exp(-\alpha x) + \frac{1}{B}(e_{\text{ox}}^i Nf(x, t) - k_r Nf(x, t)n(x, t)) = 0 \quad (31)$$

and at the stationary state it becomes

$$-\frac{\partial J(x)}{\partial x} + \alpha\Phi_0 \exp(-\alpha x) + \frac{1}{B}[e_{\text{ox}}^i - k_r n(x, t)]Nf(x) = 0 \quad (32)$$

In the case that k_2 is low enough, so that $\nu_2 = \nu_3 = \nu_4 \approx 0$, eq 28 becomes $\nu_1 \approx \nu_{\text{ox}}^i + \nu_r$ and

$$Nf \approx \frac{B\alpha\Phi_0 \exp(-\alpha x)}{k_r n + e_{\text{ox}}^i} \quad (33)$$

and eq 32 becomes

$$\frac{\partial J}{\partial x} \approx \frac{2e_{\text{ox}}^i}{k_2 n + e_{\text{ox}}^i} \alpha\Phi_0 \exp(-\alpha x) \quad (34)$$

Equation 34 is formally identical to eq 9 (dJV model), although it includes the current-doubling term. A similar behavior is obtained in the absence of current doubling.

Equation 32 can be solved with the help of eqs 16 and 29 by employing the numerical fourth-order Runge–Kutta method. To transform the initial value conditions involved in this solving method into a problem with boundary conditions, we used a shooting method. For boundary conditions in the case of illumination through the electrolyte side, we use

$$n(x=d) = 0 \quad (35)$$

$$J(x=0) = 0 \quad (36)$$

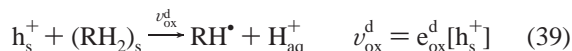
and for illumination through the substrate side, we use

$$n(x=0) = 0 \quad (37)$$

$$J(x=d) = 0 \quad (38)$$

where d is the layer thickness and $x=0$ is positioned at the illuminated layer, either at the substrate–semiconductor or at the semiconductor–electrolyte interface.²⁷

2.2. Direct Hole-Transfer Mechanism. In the case of direct hole transfer, eq 22 should be substituted with⁷



where $e_{ox}^d = k_{ox}^d[(RH_2)_s]$. The mechanism of direct hole transfer to surface-bound $(RH_2)_s$ species has been discussed elsewhere.⁷ By combining eqs 17–21, 23, 24, and 39, we obtain at the steady state

$$\nu_0 = \frac{1}{B}(\nu_1 + \nu_3 + \nu_4 + \nu_{ox}^d) \quad (40)$$

$$\nu_1 = 2\nu_2 + \nu_r \quad (41)$$

$$\nu_2 = \nu_3 = \nu_4 \quad (42)$$

$$\nu_{red}' = \nu_{ox}^d \quad (43)$$

From eq 41, the stationary concentration of holes at the surface can be determined from

$$[h_s^+] = \frac{2k_2N^2f^2 + k_rNf}{k_1N(1-f)} \quad (44)$$

and for low enough photon flux (standard experimental conditions), such that $f \ll 1$ (i.e., $[OH_s^\bullet] \ll [OH_s^-]_{in}$),⁷ we obtain

$$[h_s^+] \approx \frac{2k_2Nf^2 + k_rnf}{k_1} \quad (45)$$

Substituting eq 45 into 40, we obtain

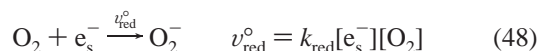
$$f = \frac{((k_1n(k_1N + e_{ox}^d))^2 + 8k_1k_2NB\alpha\Phi_0(2k_1N + e_{ox}^d)\exp(-\alpha x))^{1/2}}{4k_2N(2k_1N + e_{ox}^d)} - \frac{k_1n(k_1N + e_{ox}^d)}{4k_2N(2k_1N + e_{ox}^d)} \quad (46)$$

For the case of indirect hole transfer, the electron continuity equation, eq 30, can be rewritten considering the existence of current doubling and eq 23 as the only recombination pathway. For direct hole transfer, the electron generation rate will be $G = \alpha\Phi_0 \exp(-\alpha x) + (1/B)e_{ox}^d[h_s^+]$, and employing eq 45 for $[h_s^+]$, the continuity equation becomes

$$-\frac{\partial J}{\partial x} + \alpha\Phi_0 \exp(-\alpha x) + \frac{1}{B} \left(\frac{2e_{ox}^d k_2 N}{k_1} f^2 + \frac{k_r(e_{ox}^d n - k_1 n N)}{k_1} f \right) = 0 \quad (47)$$

Equation 47 can be solved numerically by employing the fourth-order Runge–Kutta method and a shooting method with the same boundary conditions as those used in the indirect hole-transfer case (eqs 35–38).

2.3. Effect of Dissolved O_2 . The existence of dissolved oxygen with concentrations of 10^{-3} M at most cannot be excluded under standard experimental conditions because water is photooxidized to oxygen. Therefore, the electroreduction of O_2 molecules with conduction-band electrons (eq 46) should be considered:



Equation 48 is considered to be the rate-determining step of the overall reductive process leading to H_2O as the final product.^{19–23} It should be introduced in the model as an additional recombination reaction for both direct and indirect hole transfer with the recombination rate becoming

$$R = \frac{1}{B}(k_r N f n + k_{red}[O_2]n) \quad (49)$$

3. Predictions of the Model

3.1. Dependence of $J_{x=d}$ on the Incident Photon Flux for Indirect Hole Transfer. Figure 1 shows the dependence of $J_{x=d}$ on Φ_0 for different values of the recombination rate constant k_r . Every point in Figure 1 is obtained as a numerical solution of eq 32. The log–log plot is approximately linear for the highest (correlation coefficient $r = 0.9999$) and lowest values ($r = 0.9995$) of k_r employed in the calculations, whereas for intermediate values, important deviations from the linearity appear (for instance, $r = 0.9983$ for $k_r = 10^{-11} \text{ cm}^3 \text{ s}^{-1}$). In any case, and for the sake of comparison, the slope of the linear fit is given for each set of points.

Figure 2a shows $J_{x=d}$ versus Φ_0 plots for different values of k_2 , the rate constant for the combination of OH_s^\bullet (the rate-determining step in the O_2 evolution process).²⁴ As can be seen in the Figure, the slope of the approximately linear plots increases with k_2 . Figure 2b illustrates the influence of the illumination side on the $J_{x=d}$ versus Φ_0 plot. A higher photocurrent is obtained when illumination is carried out through the substrate because more electrons are generated near the extraction contact than in the case of front-side illumination.

3.2. Dependence of $J_{x=d}$ on the Incident Photon Flux for Direct Hole Transfer. Figures 3 and 4 show $\log(J_{x=d})$ versus $\log(\Phi_0)$ plots for direct hole transfer, obtained via the numerical solution of eq 47. The behavior for direct hole transfer is similar to that observed for indirect hole transfer (Figures 1 and 2), so discrimination between direct and indirect hole transfer from the analysis of the photocurrent dependence on illumination intensity does not seem straightforward.

It is noteworthy that these numerical solutions have been obtained for the particular e_{ox}^i and e_{ox}^d values of 0.1 s^{-1} and 0.1 cm s^{-1} , respectively. Calculations for different values of these model parameters will be given elsewhere.

3.3. Influence of Dissolved Oxygen. The recombination effect via reaction 48 has been analyzed for both direct and indirect hole transfer by using the set of adjustable parameters in Figures 1 and 3. In all cases, a photocurrent intensity

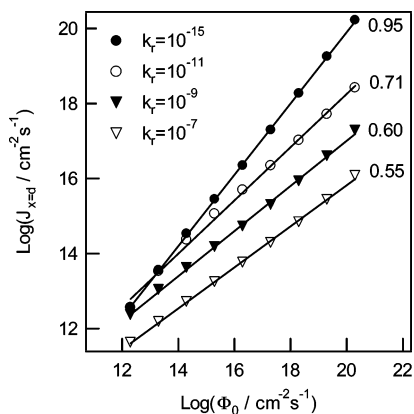


Figure 1. Theoretical logarithmic plot of $J_{x=d}$ vs Φ_0 under electrolyte-side illumination for indirect hole transfer. A low rate constant $k_2 = 10^{-15} \text{ cm}^2 \text{ s}^{-1}$ and different values of k_r ($\text{cm}^3 \text{ s}^{-1}$) are used. Other simulation parameters are $D = 10^{-5} \text{ cm}^2 \text{ s}^{-1}$, $B = 10^{-6} \text{ cm}$, $\alpha = 5 \times 10^3 \text{ cm}^{-1}$, $e_{\text{ox}}^i = 0.1 \text{ s}^{-1}$, $d = 5 \times 10^{-4} \text{ cm}$, and $k_1 = 10^{-9} \text{ cm}^3 \text{ s}^{-1}$. The slope values of a linear fit are indicated alongside.

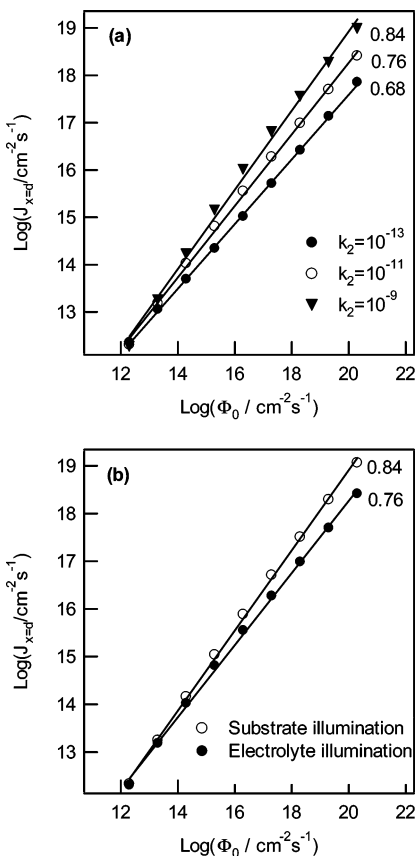


Figure 2. Theoretical logarithmic plot of $J_{x=d}$ vs Φ_0 under electrolyte-side illumination for indirect hole transfer: (a) for $k_r = 10^{-9} \text{ cm}^3 \text{ s}^{-1}$ and different k_2 values in $\text{cm}^2 \text{ s}^{-1}$; (b) comparison of the behavior obtained under electrolyte-side and substrate-side illumination for $k_2 = 10^{-11} \text{ cm}^2 \text{ s}^{-1}$ and $k_3 = 10^{-9} \text{ cm}^3 \text{ s}^{-1}$. Other simulation parameters are $D = 10^{-5} \text{ cm}^2 \text{ s}^{-1}$, $\alpha = 5 \times 10^3 \text{ cm}^{-1}$, $e_{\text{ox}}^i = 0.1 \text{ s}^{-1}$, $B = 10^{-6} \text{ cm}$, $d = 5 \times 10^{-4} \text{ cm}$, and $k_1 = 10^{-9} \text{ cm}^3 \text{ s}^{-1}$. The slope values of a linear fit are indicated alongside.

diminution was detected because of this additional recombination pathway, although the slope of the $\log(J_{x=d})$ versus $\log(\Phi_0)$ plots for both direct and indirect hole transfer showed the same behavior as that in the absence of dissolved oxygen. This is the reason that O₂ electroreduction has not been considered further in the simulation study.

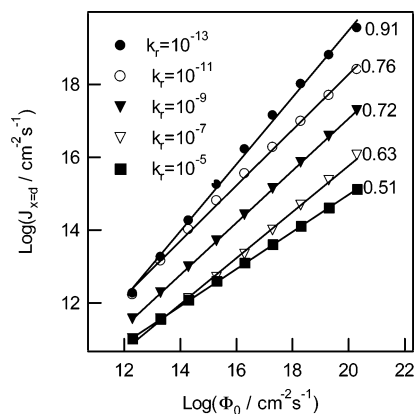


Figure 3. Theoretical logarithmic plot of $J_{x=d}$ vs Φ_0 under electrolyte-side illumination for direct hole transfer. A low rate constant $k_2 = 10^{-15} \text{ cm}^2 \text{ s}^{-1}$ and different values of k_r ($\text{cm}^3 \text{ s}^{-1}$) are used. Other simulation parameters are $D = 10^{-5} \text{ cm}^2 \text{ s}^{-1}$, $\alpha = 5 \times 10^3 \text{ cm}^{-1}$, $e_{\text{ox}}^d = 0.1 \text{ cm}^3 \text{ s}^{-1}$, $k_1 = 10^{-9} \text{ cm}^3 \text{ s}^{-1}$, $N = 10^{15} \text{ cm}^{-2}$, $d = 5 \times 10^{-4} \text{ cm}$, and $B = 10^{-6} \text{ cm}$. The slope values of a linear fit are indicated alongside.

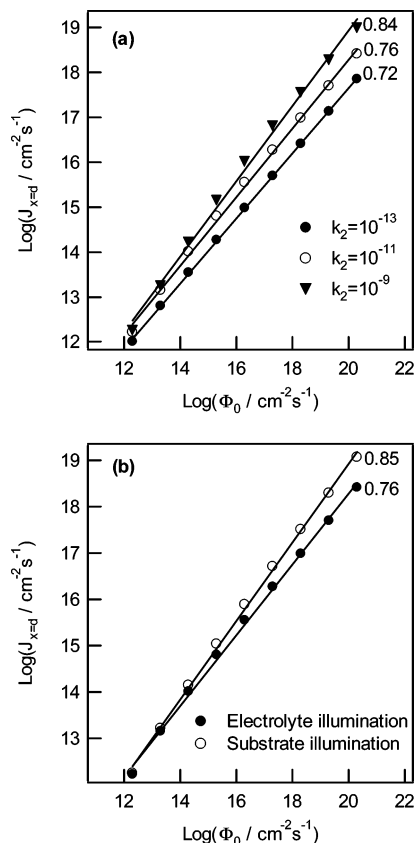


Figure 4. Theoretical logarithmic plot of $J_{x=d}$ vs Φ_0 under electrolyte-side illumination for direct hole transfer: (a) for $k_r = 10^{-9} \text{ cm}^3 \text{ s}^{-1}$ and different k_2 values in $\text{cm}^2 \text{ s}^{-1}$; (b) comparison of the behavior obtained under electrolyte-side and substrate-side illumination for $k_2 = 10^{-11} \text{ cm}^2 \text{ s}^{-1}$ and $k_3 = 10^{-9} \text{ cm}^3 \text{ s}^{-1}$. Other simulation parameters are $D = 10^{-5} \text{ cm}^2 \text{ s}^{-1}$, $\alpha = 5 \times 10^3 \text{ cm}^{-1}$, $e_{\text{ox}}^d = 0.1 \text{ cm}^3 \text{ s}^{-1}$, $N = 10^{15} \text{ cm}^{-2}$, $d = 5 \times 10^{-4} \text{ cm}$, $B = 10^{-6} \text{ cm}$, and $k_1 = 10^{-9} \text{ cm}^3 \text{ s}^{-1}$. The value of the slope of a linear fit is indicated in each curve. The slope values of a linear fit are indicated alongside.

3.4. Dependence of $[(\partial J_{x=d})/(\partial e_{\text{ox}})]_{e_{\text{ox}} \rightarrow 0}$ on the Photogeneration Rate. Recently, Villarreal et al.⁷ have developed a kinetic model that allows us to discriminate between direct and indirect interfacial hole transfer from steady-state photocurrent-intensity (expressed as $J_{x=d}$) measurements carried out with polycrystalline thin-film electrodes under current doubling and

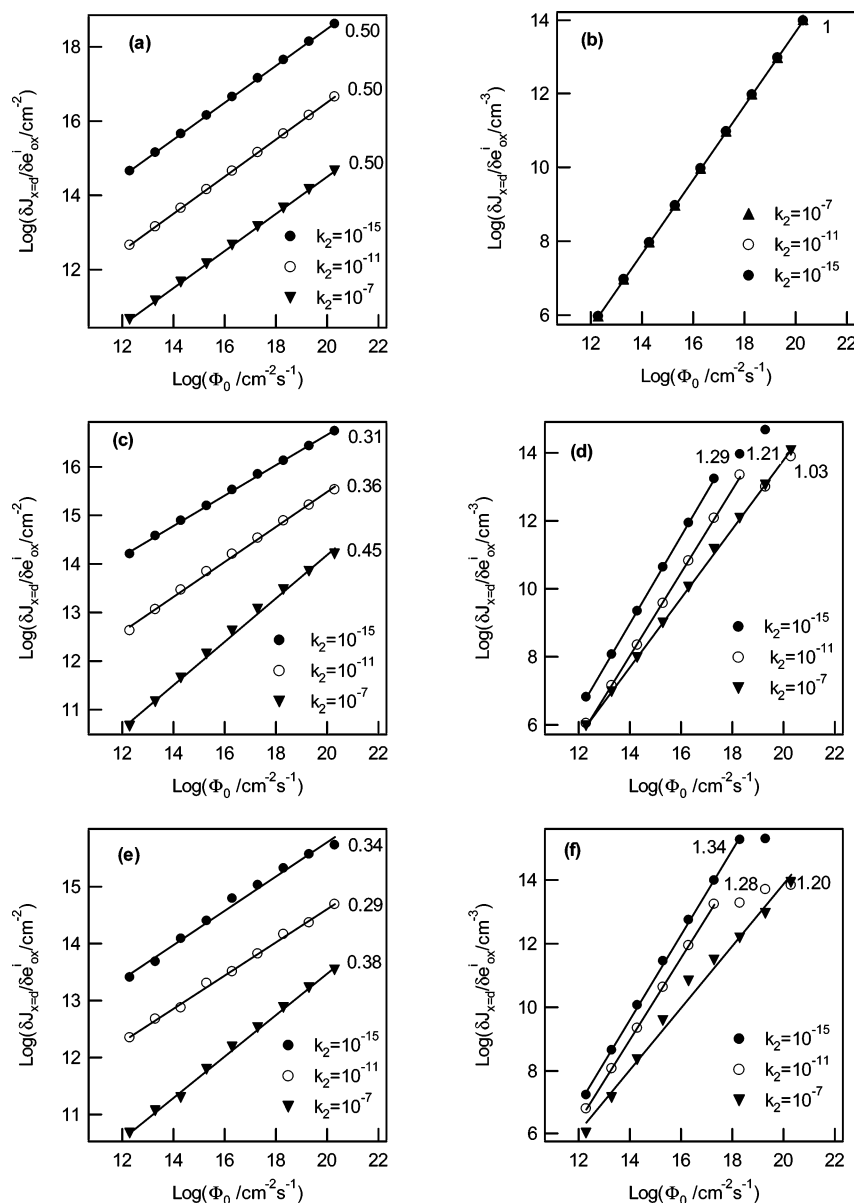


Figure 5. Theoretical logarithmic plots of $[(\partial J_{x=d})/(\partial e_{ox})]_{c_{0x}=0}$ vs Φ_0 for both indirect and direct hole transfer in the case of a nanostructured semiconductor electrode under electrolyte-side illumination for (a) indirect hole transfer with $k_r = 10^{-15} \text{ cm}^3 \text{ s}^{-1}$ and different values of k_2 ($\text{cm}^2 \text{ s}^{-1}$); (b) direct hole transfer with $k_r = 10^{-15} \text{ cm}^3 \text{ s}^{-1}$ and different values of k_2 ($\text{cm}^2 \text{ s}^{-1}$); (c) indirect hole transfer with $k_r = 10^{-9} \text{ cm}^3 \text{ s}^{-1}$ and different values of k_2 ($\text{cm}^2 \text{ s}^{-1}$); (d) direct hole transfer with $k_r = 10^{-9} \text{ cm}^3 \text{ s}^{-1}$ and different values of k_2 ($\text{cm}^2 \text{ s}^{-1}$); (e) indirect hole transfer with $k_r = 10^{-7} \text{ cm}^3 \text{ s}^{-1}$ and different values of k_2 ($\text{cm}^2 \text{ s}^{-1}$); and (f) direct hole transfer with $k_r = 10^{-7} \text{ cm}^3 \text{ s}^{-1}$ and different values of k_2 ($\text{cm}^2 \text{ s}^{-1}$). Other simulation parameters are $D = 10^{-5} \text{ cm}^2 \text{ s}^{-1}$, $\alpha = 5 \times 10^3 \text{ cm}^{-1}$, $k_1 = 10^{-9} \text{ cm}^3 \text{ s}^{-1}$, $N = 10^{15} \text{ cm}^{-2}$, $d = 5 \times 10^{-4} \text{ cm}$, $B = 10^{-6} \text{ cm}$, $e_{ox}^d = 0.1 \text{ cm s}^{-1}$, and $e_{ox}^i = 0.1 \text{ s}^{-1}$. The slope value in the low illumination range is indicated beside each curve.

in the absence of electron-hole recombination. As a discriminant test, the authors measured the illumination intensity dependence of $(\partial J_{x=d})/\{\partial[(\text{RH}_2)_{\text{aq}}]\}$ for $[(\text{RH}_2)_{\text{aq}}] \rightarrow 0$. A linear dependence of

$$\log\left(\frac{\partial J_{x=d}}{\partial[(\text{RH}_2)_{\text{aq}}]}\right)_{[(\text{RH}_2)_{\text{aq}}] \rightarrow 0}$$

on $\log(\Phi_0)$ with a slope of 0.5 was obtained for indirect hole transfer, and a slope of 1.0 was obtained for direct hole transfer. We checked the validity of a similar test for the case of nanostructured electrodes; the results are shown in Figure 5. It can be seen in Figure 5a and b that for a low enough recombination rate ($k_r = 10^{-15} \text{ cm}^3 \text{ s}^{-1}$) the behavior found is equivalent to that of polycrystalline electrodes (linearity

between

$$\log\left(\frac{\partial J_{x=d}}{\partial[(\text{RH}_2)_{\text{aq}}]}\right)_{[(\text{RH}_2)_{\text{aq}}] \rightarrow 0}$$

and $\log(\Phi_0)$, with a slope of 0.5 for indirect hole transfer and 1.0 for direct hole transfer with $r = 0.9999 - 1$). By contrast, for high enough k_r values (Figure 5c–f for $k_r = 10^{-9} - 10^{-7} \text{ cm}^3 \text{ s}^{-1}$), the linearity is lost (r ranging from 0.994 to 0.999), except for low illumination intensities, the slope of the linear region being lower than 0.5 for indirect hole transfer (Figure 5c and e) and higher than 1.0 for direct hole transfer (Figure 5d and f). It can be concluded, therefore, that the test used for dense polycrystalline electrodes is also valid for discriminating between direct and indirect hole transfer in the case of nanostructured electrodes.

4. Experimental Section: Verification of the Model

The model has been tested experimentally by using a nanostructured TiO₂ thin-film electrode. CH₃OH(aq) and HCOOH(aq) were used as model contaminants. According to Villarreal et al.,⁷ methanol becomes mainly photooxidized isoenergetically via surface-bound photogenerated OH_s[•] radicals, whereas the photooxidation of formic acid takes place via an inelastic, direct mechanism with the participation of photogenerated valence-band free holes. This behavior has been rationalized in terms

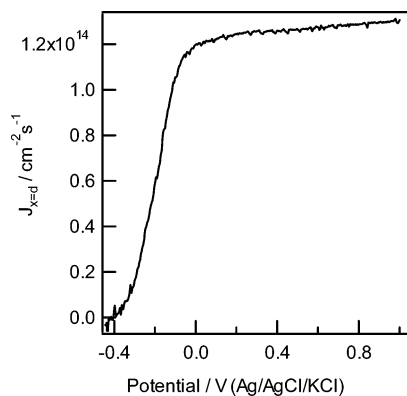


Figure 6. Experimental photocurrent intensity (expressed as an electron flux at the contact) vs applied potential plot for a nanostructured TiO₂ film electrode, prepared by electrophoresis in contact with a N₂-purged 0.5 M Na₂SO₄ (pH 3) solution under monochromatic ($\lambda = 350$ nm) electrolyte-side illumination; the scan rate is 20 mV/s.

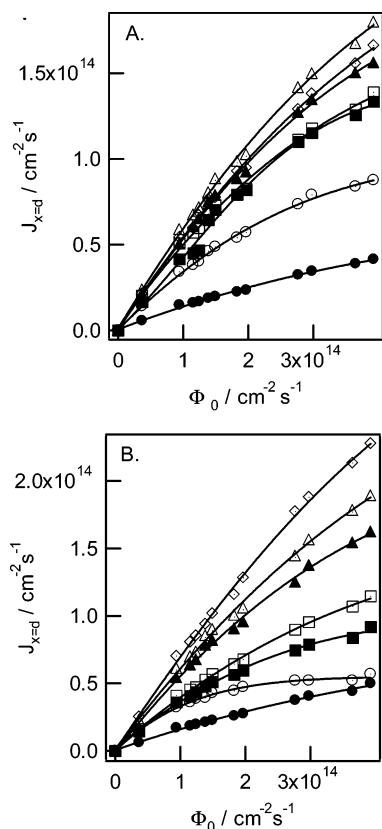


Figure 7. Experimental photocurrent intensity vs incident photon-flux plots (electrolyte-side illumination of 350 nm) under external polarization at 1 V (Ag/AgCl/KCl) for a nanostructured TiO₂ film electrode, prepared by electrophoresis, in contact with a N₂-purged 0.5 M Na₂SO₄ (pH 3) solution with different concentrations of added CH₃OH (A) and HCOOH (B): ● 0 cm⁻³, ○ 3.78 × 10¹⁷ cm⁻³, ■ 0.883 × 10¹⁸ cm⁻³, □ 1.51 × 10¹⁸ cm⁻³, ▲ 3.15 × 10¹⁸ cm⁻³, △ 6.31 × 10¹⁸ cm⁻³, and ◇ 12.6 × 10¹⁸ cm⁻³.

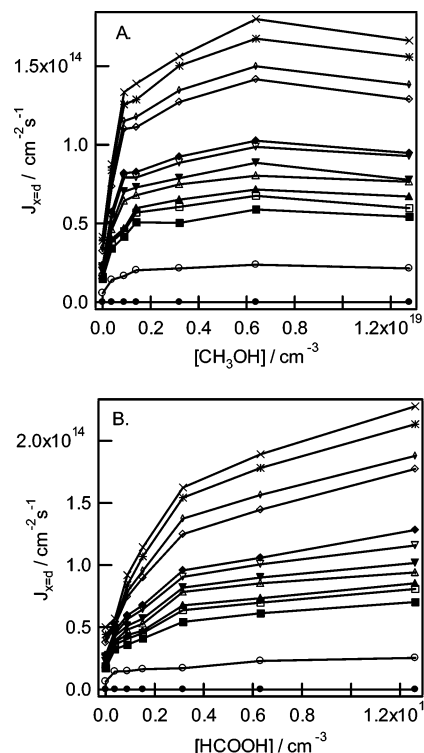


Figure 8. Experimental photocurrent intensity vs concentration of dissolved (A) methanol and (B) formic acid under external polarization of a nanostructured TiO₂ film electrode, prepared by electrophoresis, under external polarization at 1 V (Ag/AgCl/KCl) and different illumination intensities (electrolyte-side illumination of 350 nm): ● 0 cm⁻² s⁻¹, ○ 3.67 × 10¹³ cm⁻² s⁻¹, ■ 9.42 × 10¹³ cm⁻² s⁻¹, □ 1.15 × 10¹⁴ cm⁻² s⁻¹, ▲ 1.24 × 10¹⁴ cm⁻² s⁻¹, △ 1.39 × 10¹⁴ cm⁻² s⁻¹, ▼ 1.49 × 10¹⁴ cm⁻² s⁻¹, ▽ 1.83 × 10¹⁴ cm⁻² s⁻¹, ◆ 1.97 × 10¹⁴ cm⁻² s⁻¹, ◇ 2.77 × 10¹⁴ cm⁻² s⁻¹, ◇ 2.98 × 10¹⁴ cm⁻² s⁻¹, * 3.65 × 10¹⁴ cm⁻² s⁻¹, and × 3.93 × 10¹⁴ cm⁻² s⁻¹. Supporting electrolyte: N₂-purged 0.5 M Na₂SO₄, pH 3.

of the different tendencies of methanol and formic acid to interact with the TiO₂ surface in competition with water.⁷

TiO₂ layers were deposited on a F-doped SnO₂-conducting (FTO) glass substrate (Asahi Glass Co., Japan) by electrophoresis from a suspension of TiO₂ Degussa P25 (75% anatase, 25% rutile, diameter 20 nm) in methanol (1% w/v).²⁹ A potential of 10 V was applied between the FTO substrate and a gold electrode for 10 s under constant electrolyte stirring. The TiO₂ films that were obtained were finally annealed at 450 °C for 1 h in air. To minimize electron–hole recombination, we used a layer thickness of about 5 × 10⁻⁵ cm for a P25-based electrode. As we mentioned in the model section, B is on the order of the particle size (radius); therefore, for P25 films, a value of $B = 10^{-6}$ cm seems appropriate. It is worth noting that this value does not depend on the film thickness but on its structure (porosity). Photoelectrochemical measurements were performed at room temperature in a conventional three-electrode cell equipped with a fused-silica UV-transparent window. The reference electrode was a Ag/AgCl/KCl electrode with a platinum wire being used as the counter electrode. Potentiostatic measurements were performed with a computer-controlled Wenking POS2 potentiostat. All measurements were made in a deoxygenated electrolyte by N₂ bubbling for 30 min prior to and during the experiments. A N₂-purged 0.5 M Na₂SO₄ aqueous solution (adjusted to pH 3 with H₂SO₄) was used as the working electrolyte. Continuous electrolyte stirring was used to avoid mass-transfer limitations and the accumulation of photogenerated oxygen. A 150-W xenon lamp (Osram XBO) coupled to a

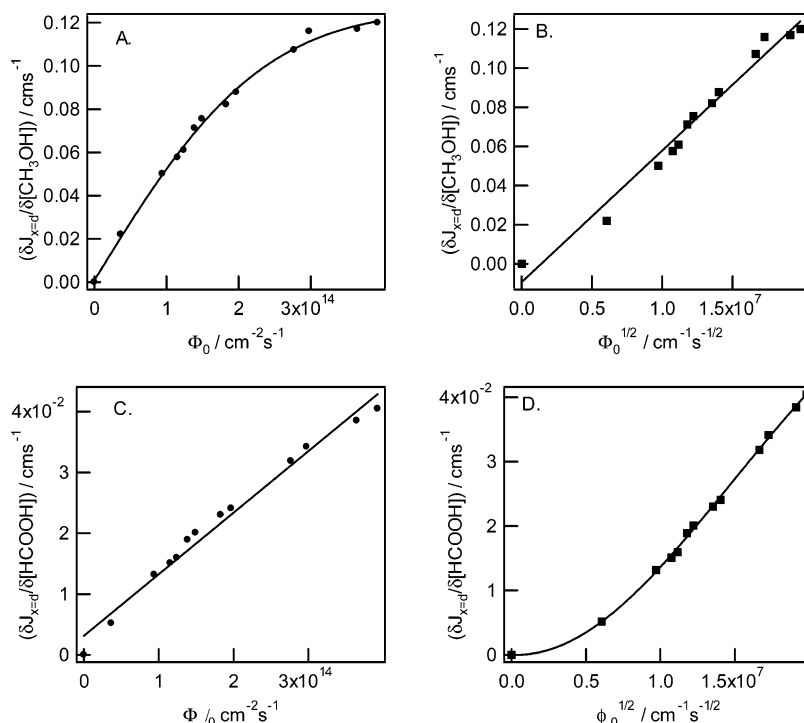


Figure 9. Plots of the slope $(\partial J_{x=d})/(\partial [RH_2]_{aq})$ for $[(RH_2)_{aq}] \rightarrow 0$ vs incident photon flux, Φ_0 ((A), (C)), and vs $\Phi_0^{1/2}$ ((B), (D)) for methanol ((A), (B)) and formic acid ((C), (D)) obtained from the experimental data in Figure 8.

monochromator (Oriel model 74000) was used as the illumination source. The intensity of the 350-nm incident light ($3.93 \times 10^{14} \text{ cm}^{-2} \text{ s}^{-1}$) was measured with an optical power meter (Oriel model 70310) equipped with a head sensor (Thermo Oriel model 71638). Different incident photon fluxes were achieved by means of neutral density filters. Steady-state photocurrent intensities were obtained after 1 min of illumination. The chemicals were purchased from the following suppliers without further purification: $\text{Na}_2\text{SO}_4 \cdot 10\text{H}_2\text{O}$ (p.a. Merck), methanol (p.a. Merck), formic acid (p.a. Merck), NaOH (pellets purissimum Panreac), and 96% H_2SO_4 (Suprapur, Merck).

Figure 6 shows the typical photocurrent–potential response of the nanostructured electrode when it is in contact with an aqueous reference electrolyte. In this case, the measured photocurrent (expressed as an electron flux) is associated with the photooxidation of water (O_2 evolution). The photocurrent onset potential appears at about -0.4 V with photocurrent saturation being reached at potentials around 0.0 V (vs Ag/AgCl/KCl). The electrode was biased at 1 V versus Ag/AgCl/KCl in further experiments to minimize electron–hole recombination. Figure 7 shows photocurrent (electron flux) versus illumination intensity (incident photon flux) plots (electrolyte-side illumination) for the nanostructured electrode in contact with the aqueous reference electrolyte containing different concentrations of methanol and formic acid, respectively (Figure 7A and B). As can be seen for $[\text{RH}_2] \geq 20 \text{ mM}$, the photocurrent is about 4 times higher than it is in the absence of dissolved RH_2 species. This photocurrent increase is due to not only a current-doubling phenomenon⁷ but also the inhibition of electron–hole recombination in the presence of the dissolved pollutant. For the case of polycrystalline electrodes, the current multiplication factor is higher for formic acid than it is for methanol. This means that in the competitive photooxidation process between the organic species and water, HCOOH is more efficiently oxidized than CH_3OH .⁷

Figure 8 shows photocurrent intensity versus $[\text{RH}_2]$ plots under different incident photon fluxes between 0.3×10^{14} and

$4 \times 10^{14} \text{ cm}^{-2} \text{ s}^{-1}$ (electrolyte side) for either CH_3OH or HCOOH added to the aqueous reference electrolyte. From this Figure, we have determined the slope $(\partial J_{x=d})/(\partial [RH_2]_{aq})$ for $[(RH_2)_{aq}] \rightarrow 0$. This slope is plotted versus Φ_0 or $\Phi_0^{1/2}$ in Figure 9.

For direct hole transfer, the surface concentration of $[(\text{RH}_2)_s]$ appears explicitly in our model, although it is not an experimental independent variable. However, $[(\text{RH}_2)_s]$ can be related to $[(\text{RH}_2)_{aq}]$ (experimental independent variable) through the adsorption isotherm. If we consider a Langmuir isotherm, then

$$[(\text{RH}_2)_s] = \frac{ab[(\text{RH}_2)_{aq}]}{1 + a[(\text{RH}_2)_{aq}]} \quad (50)$$

where a corresponds to the adsorption equilibrium constant and b corresponds to the surface concentration of adsorption sites. For low enough $[(\text{RH}_2)_{aq}]$ values, it can be considered that $1 \gg a[(\text{RH}_2)_{aq}]$ so that $[(\text{RH}_2)_s] \approx ab[(\text{RH}_2)_{aq}]$. This justifies the use of the volumetric concentration rather than the surface concentration of HCOOH when treating the experimental data of Figure 8b.

A clear difference can be observed between the plots of formic acid and methanol. Although $(\partial J_{x=d})/(\partial [RH_2]_{aq})$ depends linearly on $\Phi_0^{1/2}$ in the presence of methanol (with a correlation coefficient of 0.988), it depends linearly on Φ_0 in the presence of formic acid (with a correlation coefficient of 0.991). These results confirm the previous conclusion that formic acid is photooxidized mainly via direct hole transfer, whereas methanol is photooxidized indirectly via photogenerated hydroxyl radicals.⁷

In principle, some pollutants could degrade simultaneously via indirect and direct hole-transfer mechanisms. In fact, RH_2 species, when adsorbed, could react by capturing a valence-band free hole inelastically, whereas dissolved species present in the semiconductor–electrolyte interphase could capture a hole isoenergetically, contributing to the indirect mechanism. This would lead to a more complex diffusion equation, including

two generation and two recombination terms whose resolution would probably lead to mixed behavior. However, in practice, the direct pathway, if available, should be predominant because the reaction rate constant for direct photooxidation is (in general) higher than that for indirect photooxidations, as discussed in previous publications concerning polycrystalline thin-film electrodes and aqueous nanoparticle suspensions.^{7,28} It can be assumed, therefore, that for the illumination intensities employed commonly in both laboratory experiments and practical devices and as long as the stationary pollutant coverage is high enough (high adsorption strength), the direct hole-transfer mechanism will prevail and determine the photoelectrochemical behavior of the nanoporous thin film.

5. Conclusions

An advanced model describing the photoelectrochemical behavior of TiO₂ nanostructured photoanodes in contact with aqueous electrolytes containing dissolved pollutant species has been developed. This model takes into account the existence of mechanisms of electron–hole generation, electron transport by diffusion, electron extraction at the substrate contact, hole trapping at surface states, and hole transfer to solution via a variety of reaction paths. The diffusion equation was solved numerically to obtain the steady-state photocurrent under different experimental conditions of illumination and electrolyte composition. Following the criteria used in ref 7, we have analyzed theoretically the behavior of the slope of the log- $[(\partial J_{x=d})/(\partial e_{ox})]$ versus log(Φ_0) plot. It has been determined that under negligible recombination conditions this slope is equal to 0.5 for indirect hole transfer and 1 for direct hole transfer. This behavior allows us to discriminate between the direct and indirect hole-transfer mechanisms. This general model has been tested experimentally using thin TiO₂ nanostructured electrodes composed of P25 nanoparticles in contact with aqueous electrolytes containing either methanol or formic acid. In agreement with previous results concerning anatase polycrystalline electrodes,⁷ we have observed that methanol is photooxidized mainly via indirect hole transfer, whereas the photooxidation of formic acid takes place via a direct mechanism.

Acknowledgment. T.L.V. is grateful to the MECO (Spain) for the award of an FPU grant. This work was supported by the European Union (ICA3-CT-1999-00016) and the Ministerio de Educación y Ciencia (Spain) through project BQU2003-03737. We also acknowledge the Fundació Caixa Castelló for financial support under project P1B99-04.

Glossary

α	absorption coefficient (cm ⁻¹)
β_R	electron-trapping probability (s ⁻¹)
β_P	hole-trapping probability (s ⁻¹)
ϵ_F	driving force for the drift of photogenerated electrons (V cm ⁻¹)
Φ_0	incident photon flux (cm ⁻² s ⁻¹)
μ_n	electron mobility (cm ² s ⁻¹ V ⁻¹)
B	total volume to inner surface area ratio for the thin film (cm)
D	diffusion coefficient (cm ² s ⁻¹)
d	electrode thickness (cm)
e_{ox}^d	$k_{ox}^d[(RH_2)_s]$ (cm s ⁻¹)
e_{ox}^i	$k_{ox}^i[(RH_2)_{aq}]$ (s ⁻¹)
f	surface OH _s [•] coverage (cm ⁻²)
f_R	electron occupancy factor of the trap level denoted by R

f_h	trap-level hole-occupancy factor
G	carrier generation rate (cm ⁻³ s ⁻¹)
$J(x, t)$	electron flux (cm ⁻² s ⁻¹)
k_1	hydroxyl radicals generation constant rate (cm ³ s ⁻¹)
k_2	hydrogen peroxide generation rate constant (cm ² s ⁻¹)
k_3	HO ₂ [•] generation rate constant (cm ² s ⁻¹)
k_4	oxygen evolution rate constant (cm ³ s ⁻¹)
k_{ox}^d	direct photooxidation rate constant (cm ³ s ⁻¹)
k_{ox}^i	indirect photooxidation rate constant (cm ³ s ⁻¹)
k_r	recombination rate constant (cm ³ s ⁻¹)
k_{red}	oxygen reduction rate constant (cm ⁴ s ⁻¹)
k'_{red}	dJV model interfacial electron-transfer rate
N	initial surface-bound hydroxide ion concentration under equilibrium conditions in the dark (cm ⁻²)
$n(x, t)$	conduction-band free electron density under illumination (cm ⁻³)
n_0	conduction-band free electron density under equilibrium conditions in the dark (cm ⁻³)
$p(x, t)$	valence-band free electron density under illumination (cm ⁻³)
r	Pearsons correlation coefficient
S	internal surface area of the thin film (cm ²)
t	illumination time
V	total volume of the thin film (cm ³)
ν_0	electron–hole pairs photogeneration rate (cm ⁻² s ⁻¹)
ν_1	hydroxyl radicals photogeneration rate (cm ⁻² s ⁻¹)
ν_2	hydrogen peroxide photogeneration rate (cm ⁻² s ⁻¹)
ν_3	photooxidation rate of surface-bound photogenerated hydrogen peroxide (cm ⁻² s ⁻¹)
ν_4	photogenerated oxygen evolution rate (cm ⁻² s ⁻¹)
ν_{ox}^d	direct photooxidation rate of dissolved pollutant species (cm ⁻² s ⁻¹)
ν_{ox}^i	indirect photooxidation rate of dissolved pollutant species (cm ⁻² s ⁻¹)
ν_r	electron-hole recombination rate (cm ⁻² s ⁻¹)
ν'_{red}	electron injection rate (current doubling) (cm ⁻² s ⁻¹)
ν_{red}	oxygen reduction rate (cm ⁻² s ⁻¹)
x	film coordinate from the illuminated face

References and Notes

- (1) Pozzo, R. L.; Baltanás, M. A.; Cassano, A. E. *Catal. Today* **1997**, 39, 219.
- (2) Mills, A.; Le Hunte, S. J. *Photochem. Photobiol.*, A **1997**, 108, 1.
- (3) Fujishima, A.; Rao, T. N.; Tryk, D. A. *J. Photochem. Photobiol.*, C **2000**, 1, 1.
- (4) Tryk, D. A.; Fujishima, A.; Honda, K. *Electrochim. Acta* **2000**, 45, 2363.
- (5) Hoffmann, M. R.; Martin, S. T.; Choi, W.; Bahnemann, D. W. *Chem. Rev.* **1995**, 95, 69.
- (6) Kaneko, M.; Okura, I. *Photocatalysis Science and Technology*; Springer: New York, 2002.
- (7) Villarreal, T. L.; Gómez, R.; Neumann-Spallart, M.; Alonso-Vante, N.; Salvador, P. J. *J. Phys. Chem. B* **2004**, 108, 15172.
- (8) Ito, S.; Inoue, S.; Kawada, H.; Hara, M.; Iwasaki, M.; Tada, H. J. *Colloid Interface Sci.* **1999**, 216, 59.
- (9) Zaban, A.; Aruna, S. T.; Tirosh, S.; Gregg, B. A.; Mastai, Y. J. *Phys. Chem. B* **2000**, 104, 4130.
- (10) Bideau, M.; Claudel, B.; Dubien, C.; Faure, L.; Kazouan, H. J. *Photochem. Photobiol.*, A **1995**, 91, 137.
- (11) Mandelbaum, P.; Bilmes, S. A.; Regazzoni, A. E.; Blesa, M. A. *Sol. Energy* **1999**, 65, 75.
- (12) Ma, Y.; Qiu, J.; Cao, Y.; Guan, Z.; Yao, J. *Chemosphere* **2001**, 44, 1087.
- (13) Hagen, A.; Barkschat, A.; Dormán, J. K.; Tribustsch, H. *Sol. Energy Mater. Sol. Cells* **2003**, 77, 1.
- (14) de Jongh, P. E.; Vanmaekelbergh, D. *Phys. Rev. Lett.* **1996**, 77, 3427.

- (15) de Jongh, P. E.; Vanmaekelbergh, D. *J. Phys. Chem. B* **1997**, *101*, 2716.
- (16) Bisquert, J.; Vikhrenko, V. S. *J. Phys. Chem. B* **2004**, *108*, 2313.
- (17) Bisquert, J. *J. Phys. Chem. B* **2004**, *108*, 2323.
- (18) Fisher, A. C.; Peter, L. M.; Ponomarev, E. A.; Walker, A. B.; Wijayantha, K. G. U. *J. Phys. Chem. B* **2000**, *104*, 949.
- (19) Minero, C. *Catal. Today* **1999**, *54*, 205.
- (20) Dijkstra, M. F. J.; Panneman, H. J.; Winkelman, J. G. M.; Kelly, J. J.; Beenackers, A. A. C. M. *Chem. Eng. Sci.* **2002**, *57*, 4895.
- (21) Wang, C.-Y.; Rabani J.; Bahnemann, D. W.; Dohrmann, J. K. *J. Photochem. Photobiol., A* **2002**, *148*, 169.
- (22) Ahmed, S.; Fonseca, S. M.; Kemp, T. J.; Unwin, P. J. *J. Phys. Chem. B* **2003**, *107*, 5892.
- (23) Kesselmann, J. M.; Shreve, G. A.; Hoffmann, M. R.; Lewis, N. S. *J. Phys. Chem.* **1994**, *98*, 13385.
- (24) Salvador, P. *J. Phys. Chem.* **1986**, *89*, 3863.
- (25) Lawless, D.; Serpone, N.; Meisel, D. *J. Phys. Chem.* **1991**, *95*, 5166.
- (26) Lee, J.-J.; Coia, G. M.; Lewis, N. S. *J. Phys. Chem. B* **2004**, *108*, 5269.
- (27) Södergren, S.; Hagfeldt, A.; Olsson, J.; Lindquist, S.-E. *J. Phys. Chem.* **1994**, *98*, 5552.
- (28) Villarreal, T. L.; Gómez, R.; González, M.; Salvador, P. *J. Phys. Chem. B* **2004**, *108*, 20278.
- (29) Byrne, J. A.; Eggins, B. R.; Brown, N. M. D.; McKinney, B.; Rouse, M. *Appl. Catal., B* **1998**, *17*, 25.